Dalton Transactions

Controllable Synthesis of Up-Conversion Luminescent Gd/Tm-MOFs promising for pH-Responsive Drug Delivery and UCL/MRI Dual-Modal Imaging

Journal:	*Dalton Transactions*
Manuscript ID	DT-ART-06-2018-002436.R1
Article Type:	Paper
Date Submitted by the Author:	17-Jul-2018

Complete List of Authors:	Liu, Yana; Hubei University Zhang, Cheng; The University of Queensland, Australian Institute for Bioengineering and Nanotechnology Xu, Chen; Hubei University Lin, Caixue; Hubei University Sun, Ke; Hubei University, Wang, Jie; Hubei University Chen, Xue-Li; Department of Chemistry and Pharmaceutical Sciences, Guangxi Normal University Li, Ling; Hubei University, College of Chemistry & Chemical Engineering; Whittaker, Andrew; University of Queensland, Australian Institute for Bioengineering and Nanotechnology Xu, Hai-Bing; Hubei University, College of Chemistry & Chemical Engineering,

Controllable Synthesis of Up-Conversion Luminescent Gd/Tm-MOFs promising for pH-Responsive Drug Delivery and UCL/MRI Dual-Modal Imaging

Yana Liu[a‡], Cheng Zhang[b,c‡], Chen Xu[a], Caixue Lin[a], Keke Sun[a],Jie Wang[a], Xueli Chen[a], Ling Li[a]*, Andrew K. Whittaker[b,c]*, Hai-Bing Xu[a]*

[a.] Hubei Collaborative Innovation Center for Advanced Organic Chemical Materials, Ministry-of-Education Key Laboratory for the Synthesis and Application of Organic Function Molecules, Hubei University 430062, People's Republic of China.

[b.] Australian Institute for Bioengineering and Nanotechnology, The University of Queensland, Brisbane Qld 4072

[c.] ARC Centre of Excellence in Convergent Bio-Nano Science and Technology, The University of Queensland, Brisbane Qld 4072

‡These authors contributed equally to this work.

Corresponding Author, *Ling Li, Email: waitingll@yahoo.com; Andrew K. Whittaker: a.whittaker@uq.edu.au; Haibing Xu, Email: xhb@hubu.edu.cn

ABSTRACT

Using a facile one-step hydrothermal method, a series of metal-organic frameworks containing Gd/Tm (Gd/Tm-MOFs) were prepared successfully. Through the mutual activation of Gd^{3+} and Tm^{3+}, Gd/Tm-MOFs possessed unexpected excellent up-conversion luminescence (UCL) and superior positive magnetic resonance image (MRI). Using doxorubicin hydrochloride (DOX) as drug model, the feasibility of Gd/Tm-MOFs as multifunctional drug delivery was demonstrated. Through modifying Gd/Tm-MOFs with uniform mesoporous silica ($mSiO_2$) shells and folic acid (FA), the drug loading was improved up to 41.5 mg/g, and pH responsive drug release was climbed to 64% from 12% by regulating the pH from 5.8 to 7.4. Also, the particles were tracked by MRI, second rank of the longitudinal relaxivity (r_1) among the reported gadolinium complexes of 225.86 $mM^{-1}•s^{-1}$ was achieved. The cell imaging shows obvious blue and red luminescence with 980 nm laser excitation, and the up-conversion luminescence is unique because there is no autofluorescence from cells with 980 nm excitation. It indicates the promising application in biological application. All the experiments indicate the promising application of Gd/Tm-MOFs in diagnosis and treatment.

Keywords: Up-conversion luminescence, Metal-organic frameworks, Magnetic resonance image, Dual-modal imaging, pH responsive

1. INTRODUCTION

Due to the large specific surface areas, porous structure and easy functionalization, metal-organic frameworks (MOFs) have drawn considerable attention on potential application in drug delivery,[1–3] sensing,[4] and adsorption etc.[5]Among them, lanthanide MOFs (Ln-MOFs) possess typical lanthanide linear luminescence together with the porous structure,[6] expanding the applications to catalysis,[7] bioimaging,[8] beside sensing.[9] However, the excitation window of the traditional Ln-MOFs normally locates within the ultraviolet-visible region, leading short light penetrability depth and severe disturbance of autofluorescence background from tissues and organs,[10] thus limiting the application of Ln-MOFs in biology. Ln-MOFs with up-conversion luminescence (Up-MOFs), which can convert NIR radiations into visible radiations via a non-linear optical process,[11] has minimal autofluorescence interference, deeper NIR light penetration and slight photo-damage for vivo optical imaging and bioassay.[12,13] Therefore, design an efficient Up-MOFs is meaningful in biomedicine. Up to now, just 9 examples (Table S1) of Up-MOFs have been reported,[14–16] among them, only one example investigated the bio-application.

On the other hand, magnetic resonance imaging (MRI), which can be used for visualizing the internal structures of the body in detail, is a noninvasive diagnostic technique with excellent spatial resolution. To improve the accuracy of disease diagnosis, MRI combined with up-conversion luminescence (UCL) to afford UCL/MRI dual mode imaging contrast agent is necessary.[17-19] Although lots of composite UCL/MRI dual mode imaging contrast agents prepared by complicate and time-consuming multistep synthesis, have been reported, no more than 30 examples of homogenous materials acted as UCL/MRI dual mode imaging can be found. Among them, homogenous Up-MOFs materials with MRI have yet to be explored (Table S2). As porous structure of MOF can load and release drugs by stimulations, novel UCL/MRI dual mode MOFs, which can be acted as imaging contrast agent and a drug carrier, is hopeful to realize the integration of diagnosis and treatment.

It is essential for practical applications that strong UCL could be afforded by low excitation power density (<1 W/cm^2), thus improving the efficient UCL is a challenge. Recent progress has been achieved from co-doped crystals, such as Yb^{3+}/Tm^{3+} crystals.[20-22] To the best of our knowledge, Gd^{3+}/Tm^{3+} co-doped crystals with UCL has yet to be reported (Table S3). NIR-to-NIR even to -UV emission of Tm^{3+} also renders it potential applications in UV lasers beside bioassay.[23] Taking the photoluminescence advantages, using Tm^{3+} as an activator has received considerable attention.[24-26] It has been established that not only optimizing the UCL performance, but also excellent positive MRI by co-doping the paramagnetic gadolinium with other lanthanide ions can be afforded.[27-29] Combination the porous structure of MOFs, Gd^{3+}/Tm^{3+} co-doped Up-MOFs will become a promising multifunctional drug delivery for simultaneous bioimaging.

Inspired by the fact that Gd^{3+}/Tm^{3+} co-doped not only can improve the UCL but also can be hopefully used as UCL/MRI dual mode imaging. Herein, as shown in scheme 1, we design to use Gd^{3+} co-doped with Tm^{3+} to afford Gd/Tm-MOFs of [(Tm, Gd)(BTC)•(H_2O)•DMF]. It has been demonstrated that Gd/Tm-MOFs exhibit strong UCL (Table S1, S2, S3), when the Tm^{3+} content was regulated to 6%. Also, the structure and luminescence can be modulated through the change of synthesis condition in hydrothermal method. Taking advantage of porous structure, further modifying Gd/Tm-MOFs with uniform mesoporous silica ($mSiO_2$) shells and folic acid (FA), we realize the drug loading up to 41.5 mg/g, and pH responsive drug release to 64% at pH 5.8, and

12% at 7.4. Making use of the paramagnetic gadolinium, the Gd/Tm-MOF displays UCL/MRI dual mode imaging. Noticeably, the longitudinal relaxivity (r_1) is up to 225.86 $mM^{-1}•s^{-1}$, climbing the second ranks of the longitudinal relaxivity (r_1) among the reported gadolinium complexes. To the best of our acknowledge, this is the first example of Ln-MOF, which can be served as drug carrier with pH-responsive drug release, and UCL/MRI dual-mode imaging.

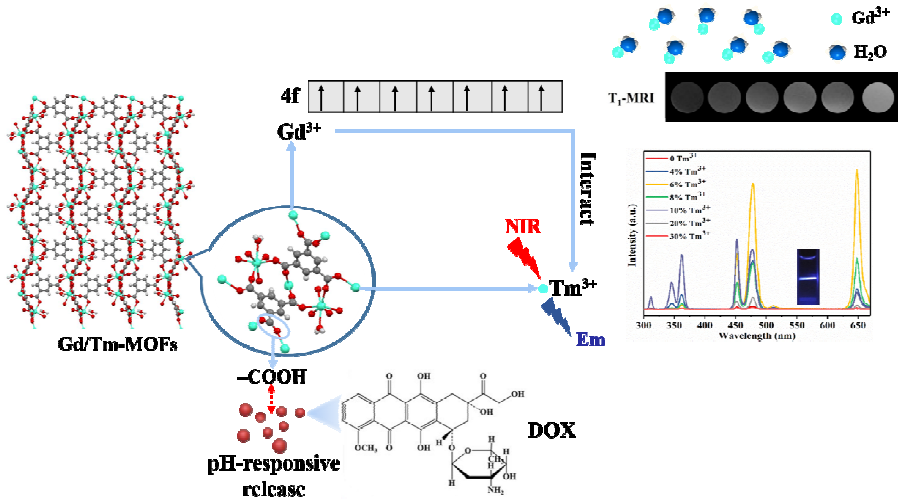

Scheme 1. Schematic illustration of the synthetic procedure. Synthetic procedure, anti-tumor drug loading and possible receptor-mediated endocytosis pathway of the targeted Gd/Tm-MOFs@$mSiO_2$-FA.

2. EXPERIMENTAL SECTION

2.1 Materials and Characterization Methods

Absolute methanol and ethanol, ammonia (28 wt% aqueous solution), tetraethyl orthosilicate (TEOS, 98%), isopropanol, N, N-dimethylformamide (DMF), polyvinylpyrrolidone (PVP), $NaAc·3H_2O$, and cetyltrimethylammonium bromide (CTAB, 99 %) were purchased from Sinopharm Chemical Reagent Co., Ltd. (Shanghai, China). $TmCl_3·6H_2O$ (99 %) from Macklin Biochemical Co., Ltd (Shanghai, China). $GdCl_3·6H_2O$ (99 %), H_3BTC, (3-aminopropyl) trimethoxysilane (APTES), N-Hydroxysuccinimide (NHS), 1-ethyl-(3-methylaminopropyl) carbodiimide hydrochloride (EDC) from Aladdin Industrial Corporation (Shanghai, China). Folic acid (FA), doxorubicin hydrochloride (DOX) from Sigma-Aldrich. Ultrapure water was used in all the preparation and characterization processes.

The power X-ray diffraction (XRD) measurements were performed using a D8 Advance X-ray diffractometer (Bruker Company, USA). Fourier transform infrared (FT-IR) spectroscopy was carried out using a Single frequency infrared spectrophotometer (PerkinElmer, USA). And scanning electron microscope images (SEM) were obtained using a JSM6510LV scanning electron microscope (JEOL, Japan). Transmission electron microscope images (TEM) were obtained via a Tecnai G20 transmission electron microscope. 752N Ultraviolet visible spectrophotometer (UV-vis) was monitored the DOX loading and release process. The UCL of materials was detected by Edinburgh Analytical Instrument (F980 fluorescence spectrometer).

2.2 Synthesis Method

Controlled Synthesis of Gd/Tm-MOFs. A mixture of $TmCl_3 \cdot 6H_2O$ (0.01 mmol), $GdCl_3 \cdot 6H_2O$ (0.09 mmol), H_3BTC (0.1 mmol), PVP (0-0.36 g), $NaAc \cdot 3H_2O$ (0-2.0 mmol), DMF (8 mL), and ultrapure water (4 mL) were added into teflon vessel, then heated several hours. The samples were washed with DMF several times. The above products were activated by methanol lasting 1 day. The final products were separated by centrifugation and dried at 60 °C for 12 h.

The different conditions of controlled synthesis of Gd/Tm-MOFs were shown in the Table 1. The amounts of additional agents (NaAc), surfactants (PVP), reaction time and reaction temperature were adjusted to obtain series Gd/Tm-MOFs samples.

Sample No.	BTC /mmol	RE^{3+} /mmol	NaAc/BTC	PVP /g	Temperature /□	Time /h
Gd/Tm-MOFs-1	0.1	0.1	1.5/1	0.09	140	24
Gd/Tm-MOFs-2	0.1	0.1	1.5/1	0.18	140	24
Gd/Tm-MOFs-3	0.1	0.1	1.5/1	0.27	140	24
Gd/Tm-MOFs-4	0.1	0.1	1/1	0.18	140	24
Gd/Tm-MOFs-5	0.1	0.1	2/1	0.18	140	24
Gd/Tm-MOFs-6	0.1	0.1	1.5/1	0.18	100	24
Gd/Tm-MOFs-7	0.1	0.1	1.5/1	0.18	160	24
Gd/Tm-MOFs-8	0.1	0.1	1.5/1	0.18	140	20
Gd/Tm-MOFs-9	0.1	0.1	1.5/1	0.18	140	28

Table 1. Different conditions of controlling synthesis Gd/Tm-MOFs

Synthesis of Gd/Tm-MOFs@mSiO$_2$-FA. This process was also completed via Stöber method. In the procedure, 0.02 g Gd/Tm-MOFs and 0.30 g CTAB were ultrasonically dispersed in a mixed solution containing 70 mL isopropyl alcohol and 10 mL ultrapure water. Then, 1.25 mL ammonia aqueous solution were added to the mixed solution. Subsequently, 20 μL TEOS and 100 μL APTES were added dropwise into the mixture. After stirring at room temperature for 6 h, the product was washed with ultrapure water and ethanol several times and dried in air at 60 □ for 12 h.

20 mg Gd/Tm-MOFs@mSiO$_2$ was washed with DMSO and dispersed in 3 mL DMSO (solution I). Parallelly, 1 mg FA and 5 μL APTES were dispersed into 3 mL DMSO to form mixture solution, then 1.1 mg NHS and 1.6 mg EDC were added into the mixture solution, solution II was formed after stirring for 2 h. Mixing solution I and II after stirring overnight, the product was centrifuged and washed with DMSO and ethanol, dried at 60 □ for 12 h.

UCL. Emission lifetimes in the solid state were determined on an Edinburgh Analytical Instrument (F980 fluorescence spectrometer) using LED laser at 980 nm excitation and the emission was detected by a thermoelectrically-cooled Hamamatsu R928P photomultiplier tube. The instrument response function at the excitation wavelength was deconvolved from the luminescence decay. The solid-state quantum yields of powder samples in sealed quartz cuvettes were measured using the integrating sphere (142 mm in diameter) of Edinburgh FLS980 Spectro-fluorophotometer (the ratio between signal to noise ca. 6000:1 by using the Raman peak

of water) with the same slit (1.9980 mm) and iris (10, the largest one is 100) in our experiments).

Cell Cytotoxicity Assessment. The biocompatibilities of the Gd/Tm-MOFs@mSiO$_2$-FA and Gd/Tm-MOFs@mSiO$_2$-FA/DOX were assessed by the 3-(4,5-dimethylthiazol-2-yl)-5-(3-carboxymethoxyphenyl)-2-(4-sulfophenyl)-2H-tetrazolium, inner salt (MTS) assay. The MCF-7 cells were grown in DMEM culture medium containing 10 % fetal bovine serum and 1% antibiotic-antimycotic (AA). The MCF-7 cells were incubated at 37.0 □ with 5% CO_2 / 95% air. The cells were seeded with Gd/Tm-MOFs@mSiO$_2$-FA (concentrations from 0 μg/mL to 12 μg/mL) on a 96-well plate in a final volume of 200 μL with 20000 cells per well for 24 h. The MTS solution (20 μL) was added into each well, and the cells were further incubated for additional 4 h. After shaking the microplate briefly on a shaker, the absorbance of treated and untreated cells at 490 nm was measured via a microplate reader. Untreated cells in medium were used as control group.

Drug Loading and Release Study. 50 mg Gd/Tm-MOFs and Gd/Tm-MOFs@mSiO$_2$-FA samples were added respectively into 20 mL of 0.1 g/L DOX solution at room temperature for 24 and 48 h under dark conditions. The Gd/Tm-MOFs/DOX and Gd/Tm-MOFs@mSiO$_2$-FA/DOX were centrifuged and washed with water to remove the excess DOX, and then dried in a vacuum drier. The drug loading capacities of two samples were calculated through the absorbance of the solution using UV-vis spectroscopy (752N Ultraviolet visible spectrophotometer) with a wavelength of 460 nm.

For the experiments of the release of DOX, 30 mg Gd/Tm-MOFs/DOX and Gd/Tm-MOFs@mSiO$_2$-FA/DOX were suspended in 20 mL of PBS (pH = 5.8 and 7.4), respectively. Both samples were gently shaken at 37 □ under dark conditions. The drug release medium (3 mL) was withdrawn for analysis by UV-vis absorption spectroscopy at 460 nm and replaced with the same volume of fresh buffer solution.

MRI. The samples were transferred to a series of 400 μL sample tubes and placed in a BrukeRhoBioSpec 94/30 USR 9.4 T small animal MRI scanner. Relaxation rates ($1/T_1$ and $1/T_2$) were measured and plotted against the concentrations of Gd. The estimation was performed using a multiple contrast spin echo sequence with the following parameters: number of slices = 1, slice thickness = 2 mm, field-of-view = 58 × 58 mm, acquisition matrix = 256 × 256, TR = 5000 ms, TE times = 30 to 300 ms with 30 ms increments.

Cell imaging. The *in vitro* optical imaging experiments were performed on an *in vivo* MS FX Pro instrument (now supplied by Bruker Corporation). Images were collected with a 980 nm excitation. MCF-7 cells employed to evaluate the properties of CLSM (Confocal Laser Scanning Microscope) of Gd/Tm-MOFs@mSiO$_2$-FA that endocytosed by the cells. MCF-7 cells were seeded on Chambered cover glass (Lab-Tek Chambered 1.0 Borosilicate Cover Glass system, Nunc). When the cell density reached 50%, particles (100 μg•mL^{-1}) were added into the medium for 24 h incubation at 37℃ under the atmosphere of 5% CO_2. Finally, the cells were washed three times with PBS (pH = 7.4) and maintained in CO_2-independent medium (Gibco) containing 10% (v/v) fetal bovine serum (Hyclone, Logan, UT). The images were taken by CLSM.

3. RESULT AND DISCUSSION

3.1 Morphology and Crystal Structure of Gd/Tm-MOFs.

The effect of amount of PVP on the morphology is shown in Figure 1(a-c). With increasing PVP, the morphology of particles tends to be well-structured and uniform. If excessive PVP dose is added, the morphology varies and becomes inhomogeneous. Owing to electrostatic repulsion effect or steric effect, the surface regulating polymeric molecule of PVP, would adsorb on the surfaces of specific crystallite, reducing their growth rate apparently and limiting crystals at micro-nano scale level.[30] The optimal amount of PVP is 0.18 g.

The effect of NaAc is shown in Figure 1(b, d, e). With increasing amounts of capping reagents NaAc, the Gd/Tm-MOFs crystals present the uniform rod-like morphology. Since the amount of NaAc controls the sample size, relatively uniform morphology can be obtained because of its improvements in coordination between RE^{3+} and organic ligands.[31] In the initially period of crystal development, the RE^{3+} bonds with the COO^- from both the organic linker of H_3BTC and NaAc,[32] hindering the crystal growth, thus leading to more nuclei. If the amount of NaAc is excessive, the rod-like crystals with non-uniform phase occurs, owing to alkalescence effect. The optimal molar ratio of NaAc/H_3BTC is 1.5/1.

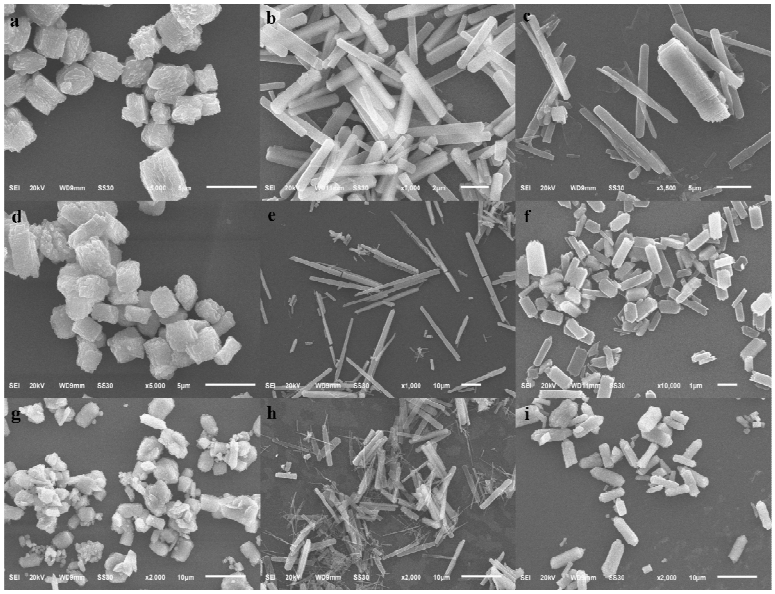

Figure 1. SEM image for the influences of PVP, NaAc, temperature and time of reaction respectively, corresponding to Gd/Tm-MOFs-1 (a) to Gd/Tm-MOFs-9 (i) in Table 1.

The effect of reaction temperature and hydrothermal time is shown in Figure 1(b, f, g), and 1(b, h, i), respectively. The crystallinity of as-prepared samples is relatively well-crystallized and uniform at low temperature. With increasing the temperature, the topology structure of samples becomes uniformity. When the temperature increases to 160 □, the particles aggregate, and the structure becomes inhomogeneity. This consequence indicates that the temperature of reaction provides the driving force that affects the movement ability of atoms and further changes the rate of crystallization and growth, thus affects the size and morphology of nanocrystals.[33] According to the experiments, the optimal temperature is 140 □.

The effect of reaction time on topologies is shown in the Figure 1(b, h, i). When heating time lasts 20 h, samples are irregular. Extending to 24 h, particles with uniform small size can be afforded. The irregular morphologies of the particles can be explained by the incomplete formation of the crystals, which results from the incompletely diffusive atoms without enough

reaction time.[34,35] Reducing reaction time is aggressively pursued as it will lead to more energy efficient process, and less requirements for synthetic equipment. In general, the crystallinity, phase purity and morphological uniformity of products are found to be affected by the temperature and time of the hydrothermal reaction. The optimal reaction time is 24 h.

In conclusion, the optimal condition is: A mixture of $TmCl_3 \cdot 6H_2O$ (0.01 mmol), $GdCl_3 \cdot 6H_2O$ (0.09 mmol), 0.15 mmol NaAc and 0.1 mmol H_3BTC, together with 0.18 g PVP, under the temperature of 140 □ for 24 h, affording the uniform Gd/Tm-MOFs particles that can be potential applied in the biotherapy. As shown in Figure 2, the UCL performance of Gd/Tm-MOFs prepared through the above optimal condition, can be modulated by the alteration of the dose of Tm^{3+}.

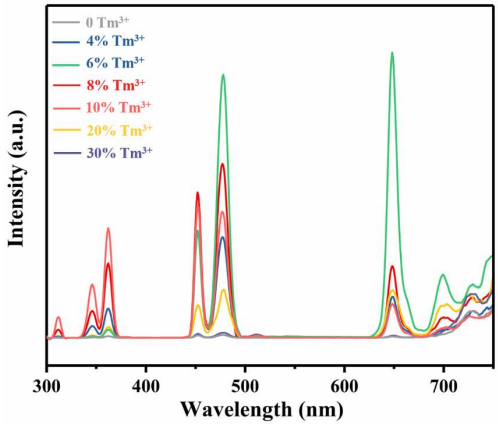

Figure 2. UCL of Up-MOF-Gd_{1-x}/Tm_x with different concentration of Tm^{3+} (0% ≤ x ≤ 30%) by excitation at 980 nm.

The Gd^{3+} ion has half full of 4f orbitals, so it just acts as the ion diluent and has effect on the emitting dopant of Tm^{3+}. The UCL spectra of the Gd/Tm-MOFs (Gd_{1-x}/Tm_x) (x is the mole fraction of Tm^{3+} in total RE^{3+}) are detected with the 980 nm excitation. As shown in Figure 2, Gd/Tm-MOFs with different Tm^{3+} concentration all exhibit characteristic emissions at 360, 450, 475, 650 and 700 nm. The peaks at 450, 475, 650 and 700 nm originate from the transition from $^1D_2 \rightarrow {}^3F_4$, $^1G_4 \rightarrow {}^3H_6$, $^1G_4 \rightarrow {}^3F_4$ and $^3F_3 \rightarrow {}^3H_6$ of Tm^{3+} ions, respectively. And a weak ultraviolet peak at 360 nm is related to $^1I_6 \rightarrow {}^3F_4$. Thus, the optimal concentration of doped Tm^{3+} ions is 6%, that favors for UCL performance. As shown in Figure S4, the lifetimes of $^1D_2$ state in $Gd_{0.94}/Tm_{0.06}$-MOFs is 379 ± 2 μs with a mono-exponential decay behavior (Figure S4), and the UCL quantum yield is ca. 0.76%. It is the first one of Up-MOFs that could give the lifetime and quantum yield (Table S1).

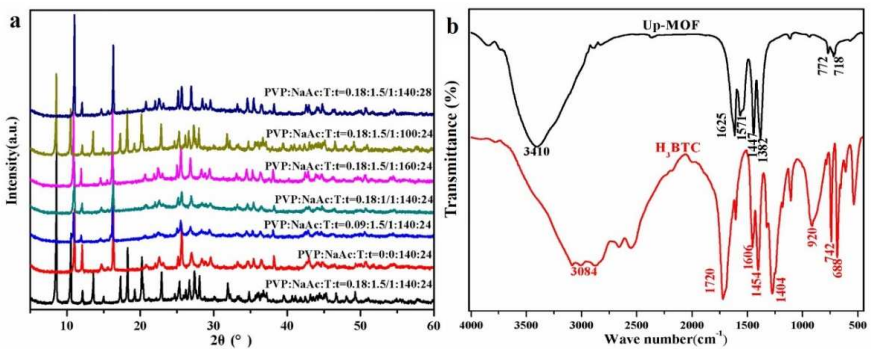

Figure 3. (a) The PXRD of Up-MOFs. PXRD peak patterns and position of optimal Up-MOF-Gd/Tm and other Up-MOFs prepared by different conditions. The T is the temperature of the reaction and the t represents for the reaction time. (b) The FT-IR absorption spectrum of H_3BTC and Up-MOFs.

The optimal morphology and UCL can be modulated through the alteration of the synthesis conditions. The successful synthesis of Gd/Tm-MOFs is further confirmed by powder XRD (Figure 3(a)) and FT-IR (Figure 3(b)). The PXRD patterns at the optimal condition is well confirmed to previous literature, indicating that Gd/Tm-MOFs is isostructural and well-indexed to the known bulk phase of JUC-32.[36,37] The PXRD peak patterns of optimal Gd/Tm-MOFs and other Gd/Tm-MOFs prepared in different conditions are various, indicating critical effects on the crystal structure of Gd/Tm-MOFs under synthesis conditions. As shown in Figure 3(b), the FT-IR spectra of the ligand H_3BTC exhibit the unbonded hydroxyl -OH groups stretching vibration at 3084 cm^{-1}, carbonyl C=O stretching at 1720 cm^{-1} of -COOH, and benzene at 1606, 1454, and 1404 cm^{-1}. Comparing with the H_3BTC, Gd/Tm-MOFs exhibits fewer absorption peaks due to the coordination bonds between metal ions Gd^{3+}/Tm^{3+} and organic ligands, including the stretching vibration band (1625 cm^{-1}) of the C=O, the vibration band (1447 cm^{-1}) of the OH groups, and the stretching band (1382 cm^{-1}), proving the formation of the coordination bonds between the carboxyl and lanthanide ions.

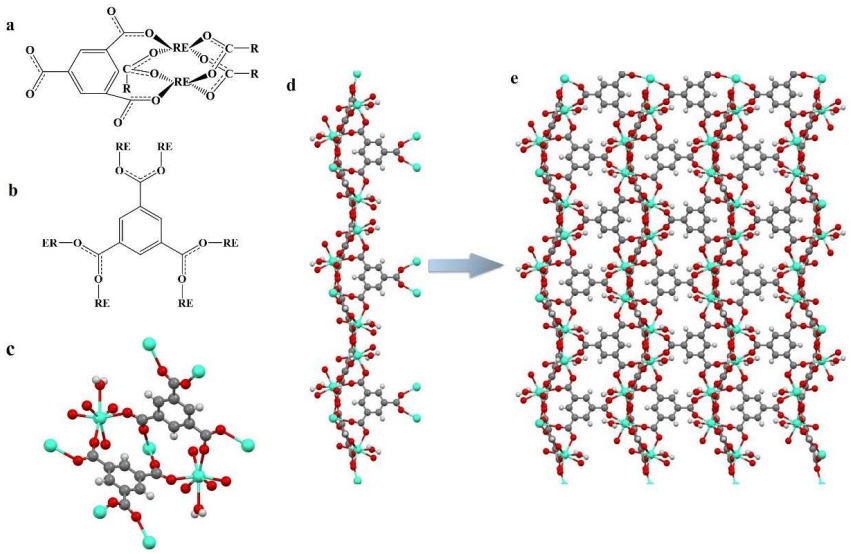

Scheme 2. (a) and (c) Two crystallographically equivalent RE ions connected by three (b) dimonodentate carboxylate groups from three different BTC ligands and two adjacent carboxylate groups of one BTC ligand. (d) 1D chains views in Up-MOFs and (e) 3D structure images of Up-MOFs with 1D channels. All hydrogen atoms and lattice water molecules are omitted for clarity. (R = BTC ligand; C atom: gray; O atom: red; rare earth ions: bright blue; H atoms are omitted for clarity).

Table 2. ICP-MS of Gd/Tm-MOFs crystal for quantitation determination of metal ions.

Elements	**Gd^{3+}**	**Tm^{3+}**

Concentration (ppm)	395.75±5%	28.17±5%

To insight the specific formation of the optimal Gd/Tm-MOFs, single-crystal X-ray diffraction is determined, as shown in Scheme 2. It shows that the formula of Gd/Tm-MOFs is RE(BTC)•(H_2O)•DMF, in which RE is Tm^{3+} and Gd^{3+}, possessing a three-dimensional framework crystallized in a chiral space group $P4_322$. The selected bond distances and bond angles of Gd/Tm-MOFs are listed in Table S4. Each building unit contains one seven-coordinated lanthanide ion (Tm^{3+} and Gd^{3+}), one BTC ligand and one water molecule. The special connection mode of RE ions leads to a one-dimensional helical inorganic chain along the [001] direction. The 1*D* inorganic chains link to each other through phenyl groups of BTC ligands along [100] and [010] directions give rise to a 3*D* framework.

As shown in Scheme 2, each Gd/Tm-MOFs building unit contains one seven-coordinated lanthanide ion (Tm^{3+} and Gd^{3+}), one BTC ligand and one water molecule. The statistics of Table 2 exhibit that the ratio of rare earth ions Gd^{3+} and Tm^{3+} is about 14:1. As shown in Scheme 2, green ball represents rare earth ions (Gd^{3+}, Tm^{3+}). Two crystallographically equivalent RE ions are connected by three dimonodentate carboxylate groups from three different BTC ligands and two adjacent carboxylate groups of one BTC ligand (Scheme 2(a-c)). All these confirm the successfully co-doping of Gd^{3+} and Tm^{3+}. Even if the structure has been reported, but the co-doping of Gd^{3+} and Tm^{3+} is never prepared(Table S1). Co-doping will make the materials unexpected performance, which can be confirms by the UCL performance with different concentration of Tm^{3+} (Figure 2). Single Gd^{3+} can not give UCL, and with the addtion of Tm^{3+}, the intensity of UCL becomes strong. But when the amount of Tm^{3+} exceeds 6%, the intensity decreases. It can be explained the UCL of Tm^{3+} is weak itself, when the Tm^{3+} keeps increasing, the UCL inclines to show the weak intensity of Tm^{3+} itself. Only with the optimal ratio of Gd^{3+} : Tm^{3+}, there is the strongest UCL intensity, indicating the mutual activation of Gd^{3+} and Tm^{3+}. Therefore, co-doping of Gd^{3+} and Tm^{3+} is meaningful.

3.2 Characterization of Gd/Tm-MOFs@$mSiO_2$-FA

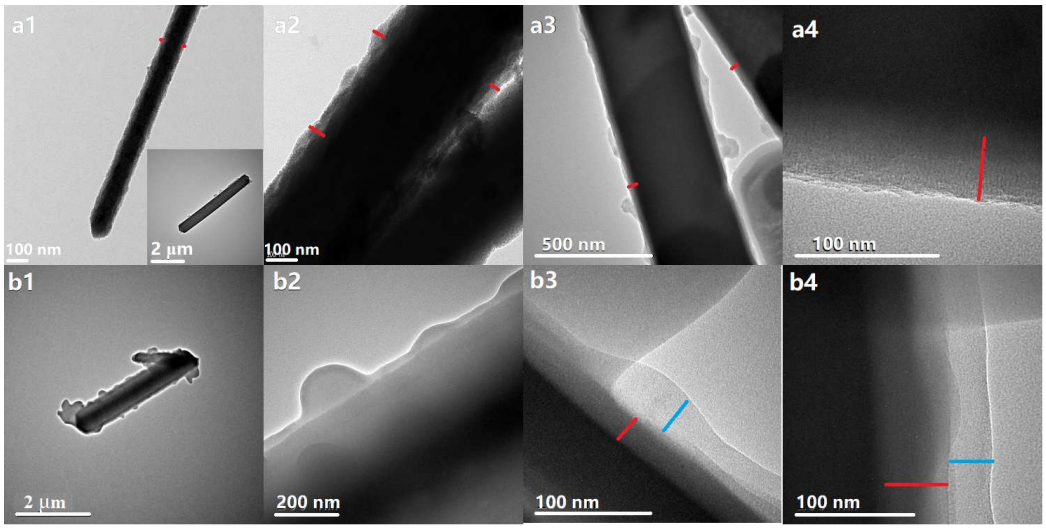

Figure 4. The TEM images of Gd/Tm-MOFs@mSiO$_2$ (a1-a4) and Gd/Tm-MOFs@mSiO$_2$-FA (b1-b4).

On basis of the Gd/Tm-MOFs with the optimal morphology and UCL, Gd/Tm-MOFs@mSiO$_2$ and Gd/Tm-MOFs@mSiO$_2$-FA are prepared. The successful silica coating and folic acid modification are proved by TEM. As shown in Figure 4 (a1-a4), Gd/Tm-MOFs@mSiO$_2$ shows clear core-shell structure, which is comprised with Gd/Tm-MOFs particles as core and about 40 nm silica as shell (red line). The result is consistent with the DLS determination (Figure S5). The DLS suggests that the average width of Gd/Tm-MOFs was 450 nm and the width of Gd/Tm-MOFs@mSiO$_2$ was around 530 nm approximately. It demonstrates that the thickness of mesoporous SiO$_2$ shell was about 40 nm. In comparison, the TEM images of Gd/Tm-MOFs@mSiO$_2$-FA clearly shows double shell (red line and blue line), indicating that the surface of silica shells is covered with new attachment (Figure 4 b1-b4).

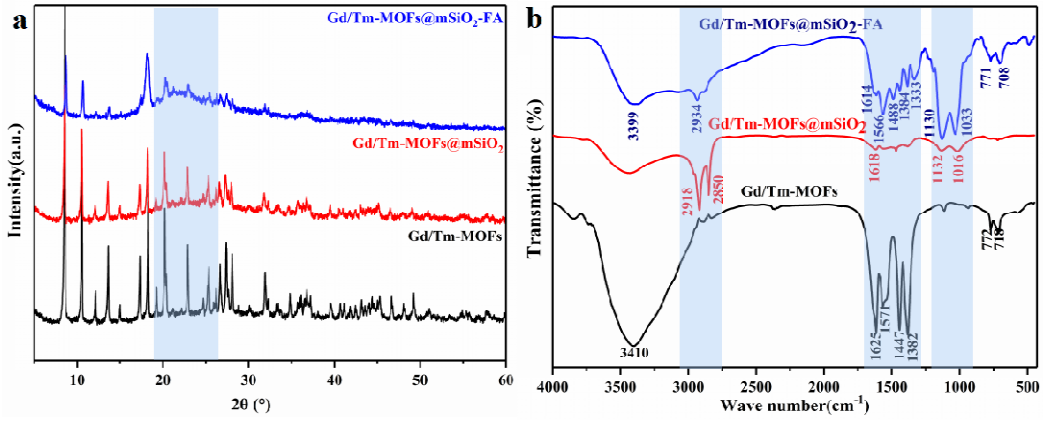

Figure 5. The PXRD patterns (c) and FT-IR spectrum (d) of Gd/Tm-MOFs, Gd/Tm-MOFs@mSiO$_2$ and Gd/Tm-MOFs@mSiO$_2$-FA.

The successful silica coating and folic acid modification can be further proved by PXRD patterns and FT-IR spectrum . As shown in PXRD patterns (Figure 5(a)), the wide peak at 2θ =

22°, and the lower peak intensity proves that SiO_2 and FA are coated successfully on the surface of Gd/Tm-MOFs. EDS further proves the presence of SiO_2 and FA (Figure S6). In FT-IR spectra (Figure 5(b)), two strong bands at 2918 and 2850 cm^{-1} of Gd/Tm-MOFs@$mSiO_2$ are observed compared with Gd/Tm-MOFs, which can be associated with the asymmetric and symmetric stretching vibrations of -NH_2 on the surface of $mSiO_2$. And the peak at 1016 cm^{-1} is contributed to the symmetric stretching vibrations of Si-O-Si. It suggests that mesoporous SiO_2 shell modified with -NH_2 are coated successfully on the surface of Gd/Tm-MOFs. After modified with FA, the characteristic adsorption peaks of Gd/Tm-MOFs@$mSiO_2$-FA located among 1614 to 1033 cm^{-1} prove the presence of FA.

3.3 Cell viability

To evaluate the feasibility of Gd/Tm-MOFs@SiO_2-FA as a multifunctional drug carrier, the cell viability of Gd/Tm-MOFs@SiO_2-FA at different concentrations to MCF-7 cells are evaluated by MTS assay (Figure 6). The MCF-7 cells treated with Gd/Tm-MOFs@SiO_2-FA show negligible cell death even the concentration up to 12 μg/mL, thus the transport vehicles of Gd/Tm-MOFs@SiO_2-FA particles are biocompatible, rending them suitable to be applied in cells. However, if the concentration further climbs, the Gd/Tm-MOFs@SiO_2-FA/DOX particles show increasing toxic effect against MCF-7 cells, it is found that about 54% MCF-7 cells can be killed at 12 μg/mL of Gd/Tm-MOFs@SiO_2-FA/DOX with an equivalent DOX concentration of 0.498 μg/mL. Since the unique interaction between the FA on the Gd/Tm-MOFs@SiO_2 surface and the folate receptors in the MCF-7 cell membrane, support folate receptor mediated endocytosis.[43]

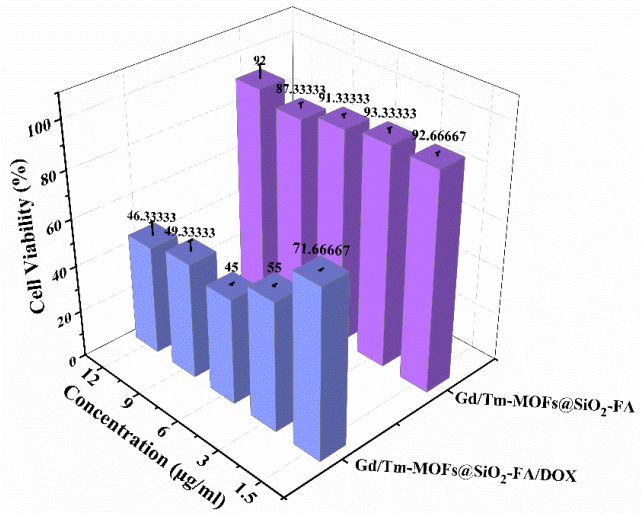

Figure 6. *In vitro* cell viability after incubation for 24 h with Gd/Tm-MOFs@SiO_2-FA and Gd/Tm-MOFs@SiO_2-FA/DOX at different concentrations to MCF-7 cancer cells measured by MTT assay.

3.4 Drug Delivery

Further to explore the performance for drug delivery, the drug loading and release is discussed. As shown in Figure 7, after modifying Gd/Tm-MOFs with uniform mesoporous silica ($mSiO_2$) shells and folic acid (FA) to form Gd/Tm-MOFs@$mSiO_2$-FA, the capacity of DOX loading becomes much better. For instance, the capacity of the drug loading on the latter reaches from 10.6 to 41.5 mg/g, when the incubation time lasts from the first 24 to 48 hours (Figure 7 (a)). In parallel,

the one on the former only reaches to 8.3 mg/g after 48 h. This could occur because the surface area of the latter is larger (43.71 m^2/g) than the former (22.48 m^2/g) (Figure S7). As a result, meso-porous silica layer is favorable for improving the drug loading.

The DOX release from Gd/Tm-MOFs and Gd/Tm-MOFs@$mSiO_2$-FA at pH 5.8 are both faster than that at pH 7.4, as depicted in Figure 7 (b). It indicates pH-responsive drug release. As for Gd/Tm-MOFs, at the first ten hours, DOX release reaches to 30% at pH 5.8, and the release velocity slows down till 60 h, inducing the total drug release efficiency to 40% at pH 5.8 and 18% at pH 7.4. Interestingly, the DOX release capacity reaches to 64% at pH 5.8 and 12% at pH 7.4 from Gd/Tm-MOFs@$mSiO_2$-FA. Compared with reported pH responsive materials recently (Table S5), the values (52%) is beyond average. Thus, the Gd/Tm-MOFs@$mSiO_2$-FA particles shows better pH responsive release, making it suitable for multifunctional drug delivery.

The pH responsive release of Gd/Tm-MOFs is because the decomposition of MOFs in acid buffer[43]. The mechanism of pH responsive DOX release from Gd/Tm-MOFs@$mSiO_2$-FA is discussed in Figure 7 (c, d). At pH 7.4, the release of DOX molecule is hindered owing to the formation of hydrogen bond among the -OH of DOX and -NH_2 groups of amino from the modified silica shell. At pH 5.8, the -OH and -NH_2 groups are protonated and would repel each other, releasing the DOX molecules. In comparison, the drug release rate of Gd/Tm-MOFs@$mSiO_2$-FA is higher than Gd/Tm-MOFs at pH 5.8. The main reason is probably that DOX loading of MOFs depends on the physical adsorption of the porous structure, while the loading of Gd/Tm-MOFs@$mSiO_2$-FA depends not only on the physical adsorption of MOFs but also on the chemical adsorption (hydrogen bond) between the -OH of DOX and -NH_2 of amino from the modified silica shell. At pH 5.8, the chemical adsorption of silica shell is broken, at the same time, the core MOFs also begins decomposing, and thus the two effects cause the drug to be released faster. Therefore, silica coating not only helps to improve the drug loading, but also contributes to drug release with better pH-response.

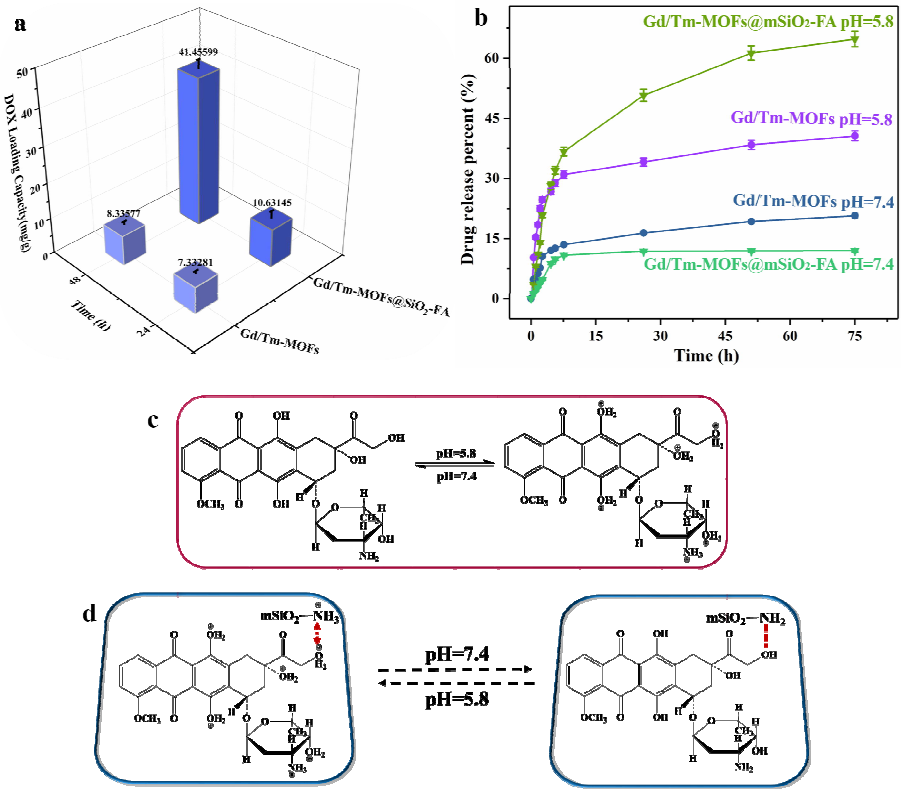

Figure 7. Drug loading capacity (a) and drug release profiles (b) of Gd/Tm-MOFs and Gd/Tm-MOFs@mSiO_2-FA; and schematic of pH-responsive release of DOX from Gd/Tm-MOFs@mSiO_2 at different pH values (c, d).

The pH-responsive drug release is in accordance with the result of cell viability. Since the DOX can be successfully released in acid environment, the released DOX from Gd/Tm-MOFs@mSiO_2-FA can kill the MCF-7 cells. The absolute drug release from Gd/Tm-MOFs@mSiO_2-FA/DOX in acid environment is 52% with 7.08 μg/mL DOX, which is beyond the killing effect (53%) of 0.498 μg/mL DOX. Therefore, through the regulating the supply of Gd/Tm-MOFs@mSiO_2-FA/DOX, we can achieve the effective cure for cancer.

3.5 UCL and MRI

As shown in Figure 8 (a), although the SiO_2 shell and FA layer weaken the emission, inducing the UCL intensity of Gd/Tm-MOFs@mSiO_2-FA inferior to Gd/Tm-MOFs, five distinct peaks at 360 nm, 450 nm, 475 nm, 650 nm, and 700 nm of Gd/Tm-MOFs@SiO_2-FA are observed by excitation at 980 nm, providing the basis for the UCL imaging.

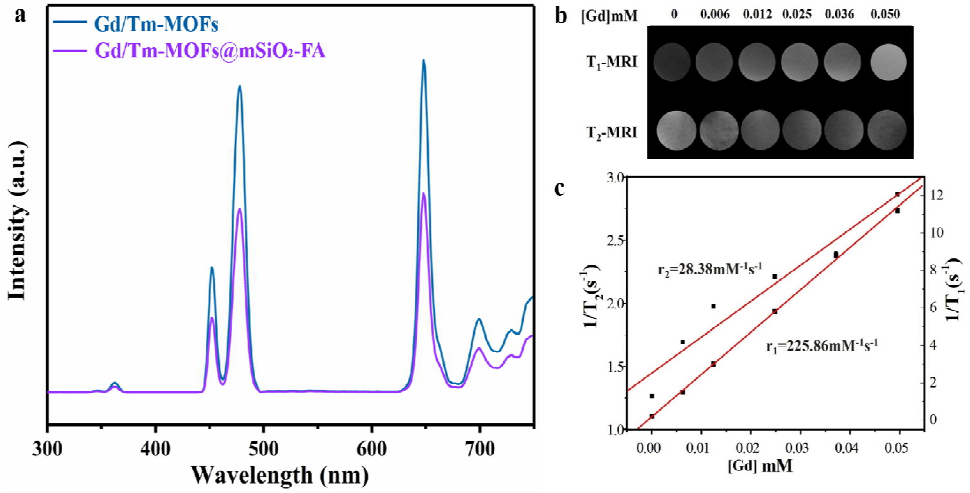

Figure 8. (a) UCL spectra of Gd/Tm-MOFs and Gd/Tm-MOFs@mSiO$_2$-FA by excitation of 980 nm; (b) T_1 and T_2-weighted MRI and relaxivity plots for aqueous solutions of the Gd/Tm-MOFs@SiO$_2$-FA nanoparticles at 9.4 T.

To evaluate the feasibility of Gd/Tm-MOFs@SiO$_2$-FA for MRI, the longitudinal and transverse relaxivity are measured. The reciprocal values of relaxation times are plotted as a function of Gd concentration. It can be seen from Figure 8 (b) that MRI shows apparently dose-dependent contrast enhancements, which indicates that the potential applications of Gd/Tm-MOFs@SiO$_2$-FA as T_1 and T_2 contrast agents. The accurate effect of transverse relaxation is represented by the longitudinal (r_1) and transverse relaxivity (r_2). The relationship of the inverse relaxation time $1/T_1$ and $1/T_2$ versus Gd concentrations is presented in Figure 8 (c), the relaxivity values are determined to be r_1 = 225.86 mM^{-1}•s^{-1} and r_2 = 28.38 mM^{-1}•s^{-1}, respectively. For the MRI, the r_2 / r_1 ratio is an important criterion to confirm whether a given contrast agent is either T_1 or T_2-dominated MRI contrast agent. The high r_2 / r_1 ratio (> 8) leads to a T_2-dominated contrast, while the lower ratio (< 5) results in a T_1-dominated contrast.[38] Thus, Gd/Tm-MOFs@SiO$_2$-FA (r_2 / r_1 ~ 0.126) is an excellent T_1-weighted MRI contrast agent. Compared with reported materials recently (Table S6), the Gd/Tm-MOFs@SiO$_2$-FA have a remarkably large r_1 relaxivity. As illustration in crystal structure, seven-coordinated lanthanide ion (Tm^{3+} and Gd^{3+}) favoring the second coordination sphere interactions between H_2O or plenty of -OH on the surface of mesoporous silica shell and the empty orbits of Gd^{3+}.[39] Also, large positive magnetic susceptibility anisotropy of Tm^{3+} can create more opportunities to combine with H_2O or -OH. All the facts improve the r_1 value [40-41] as the second rank among the reported gadolinium complexes (Table S6). It is interesting that the large r_1 value is also the result of the mutual activation of Gd^{3+} and Tm^{3+}. Combination the UCL and MRI, the Gd/Tm-MOFs@SiO$_2$-FA can be potentially used for UCL/MRI dual mode imaging.

3.6 Cell imaging

The cellular uptake process by MCF-7 cells is examined by the confocal laser scanning microscopy (CLSM) with 980 nm laser. MCF-7 cells are incubated with Gd/Tm-MOFs@mSiO$_2$-FA (100 μg•mL^{-1}) for 24 h. As shown in Figure 9, comparing with blank group, it can be seen that the cells incubated with Gd/Tm-MOFs@mSiO$_2$-FA show a obvious blue (475 nm) and red (650 nm) luminescence signal with 980 nm laser excitation (Figure 1(b, c)), and no autofluorescence background from the MCF-7 cells is observed. It proves the particles can be taken up and stay within the cells after incubation. In addition, the The imaging results demonstrate that the Gd/Tm-MOFs@mSiO$_2$-FA can be used for cell imaging, and the UCL

imaging will not be affected by autofluorescence of cells.

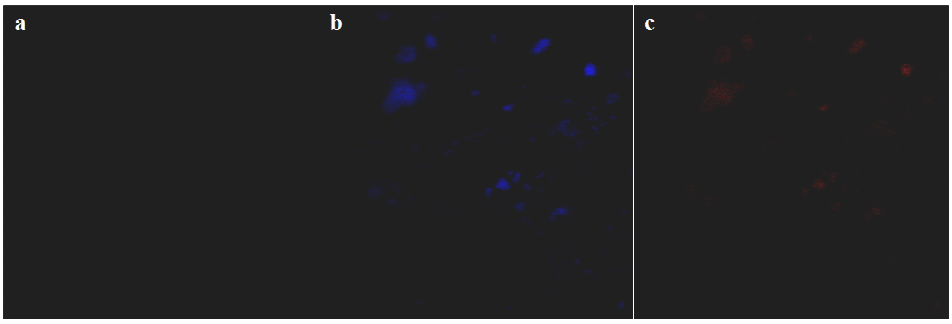

Figure 9. In vitro UCL images of MCF-7 cells using the Gd/Tm-MOFs@mSiO$_2$-FA(a, b, c) as luminescent probe under excitation with 980 nm laser (a are blank group without dyeing).

4. CONCLUSION

In summary, the first example of Gd/Tm-MOFs with UCL and MRI have been successfully fabricated via a relatively facile and simple one-step solvothermal method. The optimal conditions, such as capping reagent, surfactant, reaction time, reaction temperature, and the mole fraction of Tm^{3+}, have been discussed. It has been demonstrated the strongest UCL with the lifetime of 379 ± 2 μs and the quantum yield of 0.76 % could be achieved under the concentration of doped Tm^{3+} ions of 6%. Superior drug loading and pH responsive drug release, and second rank of the longitudinal relaxivity (r_1) among the reported gadolinium complexes was achieved by modifying with uniform mesoporous silica (mSiO$_2$) shells and folic acid (FA). The unexpected excellent performance are the results of mutual activation of Gd^{3+} and Tm^{3+}. All these facts render multifunctional Gd/Tm-MOFs promising to be served as drug carrier and pH-responsive drug release, and UCL/MRI dual-mode imaging, providing a new strategy for accurate cancer treatment in near future.

ACKNOWLEDGEMENTS

This work was supported by Natural Science Foundation of Hubei Province (No.2017CFB530), Wuhan Morning Light Plan of Youth Science and Technology (No.2017050304010282) and the National Natural Science Foundation of China (No.51302071). This work was also supported by the National Science Foundation of China (No. 21571165). The authors acknowledge the Australian Research Council (CE140100036, DP0987407, DP110104299, LE0775684, LE0668517, and LE0882357) and the National Health and Medical Research Council (APP1021759) for funding of this research. The Australian National Fabrication Facility, Queensland Node, is also acknowledged for access to some items of equipment. The National Imaging Facility is acknowledged for the access of ClinScan. C. Z. acknowledges the University of Queensland for his Early Career Researcher Grant (UQECR1720289).

REFERENCE

1. J. Zhuang, C. H. Kuo, L. Y. Chou, D. Y. Liu, E. Weerapana, C. K. Tsung, *ACS Nano*, **2014**, *8*, 2812.
2. L. Li, Y. N. Liu, K. K. Sun, Y. He, L. Liu, *Mater. Lett.* **2017**, *197*, 196.
3. K. K. Sun, L. Li, X. L. Yu, L. Liu, Q. T. Meng, F. Wang, R. Zhang, *J. Colloid. Interface. Sci.* **2017**, *486*, 128.

4. M. Rieger, M. Wittek, P. Scherer, S. Löbbecke, K. Müller□Buschbaum, *Adv. Func. Mater.* **2017**, *28*, 1704250.
5. Z. Rao, K. Feng, B. B. Tang, P. Y. Wu, *ACS Appl. Mat. Interfaces.* **2017**, *9*, 2594.
6. J. Rocha, L. D. Carlos, F. A. A. Paz, D. Ananias. *Chem. Soc. Rev.* **2011**, 42, 926.
7. S. Dasari, S. Singh, S. Sivakumar, A. K. Patra, *Chem. Eur. J.* **2016**, *22*, 17387.
8. H. Weng, B. Yan, *Sens. Actuators, B* **2016**, *228*, 702.
9. J. R. Choi, T. Tachikawa, M. Fujitsuka, T. Majima, *Langmuir.* **2010**, *26*, 10437.
10. S. Ma, D. Yuan, X. S. Wang, H. C. Zhou, H. C. Zhou, *Inorg. Chem.* **2009**, *48*, 2072.
11. M. Wang, G. Abbineni, A. Clevenger, C. Mao, S. Xu, *Nanomed. Nanotechnol. Biol. Med.* **2011**, *7*, 710.
12. M. Lin, Y. Gao, F. Hornicek, F. Xu, T. J. Lu, M. Amiji, Z. Duan, *Adv. Colloid Interface Sci.* **2015**, *226*, 123.
13. S. W. Hao, G. Y. Chen, H. L. Qiu, C. Xu, R. W. Fan, X. B. Meng, C. H. Yang, *Mater. Chem. Phys.* **2012**, *137*, 97.
14. X. D. Zhang, B. Li, H. P. Ma, L. M. Zhang, H. F. Zhao, *ACS Appl. Mat. Interfaces.* **2017**, *9*, 2594.
15. D. F. Weng, X. J. Zheng, L. P. Jin, *Eur. J. Inorg. Chem.* **2006**, 4184.
16. K. L. Wong, W. M. Kwok, W. T. Wong, D. L. Phillips, K. W. Cheah, *Angew. Chem.* **2004**, *116*, 4759.
17. A. N. Generalova, B. N. Chichkov, E. V. Khaydukov, *Adv. Colloid Interface Sci.* **2017**, *245*, 1.
18. C. L. Chen, J. H. Liu, Y. Chen, C. G. Li, X. M. Liu, H. Huang, C. Liang, Y. Lou, Z. Shi, S. H. Feng, *ACS Appl. Mater. Interfaces* **2017**, *9*, 5748.
19. W. Yuan, D. P. Yang, Q. Q. Su, X. J. Zhu, T. Y. Cao, Y. Sun, Y. Dai, W. Feng, F. Y. Li, *Adv. Func. Mater.* **2016**, *26*, 8631.
20. S. H. Fan, G. J. Gao, D. Busko, Z. Q. Lin, S. K. Wang, X. Wang, S. Y. Sun, A. Turshatov, B. S. Richards, H. T. Sun, L. L. Hu, *J. Mater. Chem. C* **2017**, *5*, 9770.
21. Y. D. Yang, P. W. Zhou, W. Xu, S. Xu, Y. D. Jiang, X. Chen, H. W. Song, *J. Mater. Chem. C* **2016**, *4*, 659.
22. H. Q. Yan, X. Q. Chen, J. Shi, Z. F. Shi, W. Sun, Q. Lin, X. H. Wang, Z. H. Dai, *Mater. Sci. Eng., C* **2017**, *71*, 51.
23. V. Kale, M. Lastusaari, J. Holsa, T. Soukka, *RSC Adv.* **2015**, *5*, 35858.
24 H. Q. Chen, F. Yuan, S. Z. Wang, J. Xu, Y. Y. Zhang, L. Wang, *Analyst* **2013**, *138*, 2392.
25. L. N. Sun, X. Q. Ge, J. L. Liu, Y. N. Qiu, Z. W. Wei, B. Tian, L. Y. Shi, *Nanoscale* **2014**, *6*, 13242.
26. A. Xia, Y. Gao, J. Zhou, C. Y. Li, T. S. Yang, D. M. Wu, L. M. Wu, F. Y. Li, *Biomaterials* **2011**, *32*, 7200.
27. Y. Cao, M. Liu, K. C. Zhang, G. Y. Zu, Y. Kuang, X. Y. Tong, D. S. Xiong, R. J. Pei, *Biomacromolecules* **2017**, *18*, 150.
28. R. Kumar, M. Nyk, T. Y. Ohulchanskyy, C. A. Flask, P. N. Prasad, *Adv. Funct. Mater.* **2009**, *19*, 853.
29. J. Schmitt, V. Heitz, A. Sour, F. Bolze, P. Kessler, L. Flamigni, B. Ventura, C. S. Bonnet, Ê. Tûth, *Chem. Eur. J.* **2016**, *22*, 2775.
30. F. Z. Haque, M. R. Parra, H. Siddiqui, N. Singh, N. Singh, P. Pandey, K. M. Mishra, *Opt. Spectrosc.* **2016**, *120*, 408.
31. H. L. Guo, Y. Z. Zhu, S. L. Qiu, J. A. Lercher, H. J. Zhang, *Adv. Mater.* **2010**, *22*, 4190.
32. T. Tsuruoka, S. Furukawa, Y. Takashima, K. Yoshida, S. Isoda, S. Kitagawa, *Angew. Chem.* **2009**, *48*, 4739.
33. F. Z. Liu, X. Shao, Y. B. Yin, L.M. Zhao, Q. Z. Sun, Z. W. Shao, X. H. Liu, X. H. Meng, *J. Rare Earths* **2011**, *29*, 97.

34. T. Adschiri, H. A. Yukiya, K. Arai, *Ind. Eng. Chem. Res.* **2000**, *39*, 4901.
35. H. Li, M. M. Sadiq, K. Suzuki, P. Falcaro, A. J. Hill, M. R. Hill, *Chem. Mater.* **2017**, *29*, 6186.
36. Z. Y. Li, G. S. Zhu, G. W. Lu, S. L. Qiu, X. D. Yao, *J. Am. Chem. Soc.* **2010**, *132*, 1490.
37. X. D. Guo, G. S. Zhu, Z. Y. Li, F. X. Sun, Z. H. Yang, S. L. Qiu, *Chem. Commun.* **2006**, *30*, 3172.
38. Y. Chen, K. L. Ai, J. H. Liu, X. Y. Ren, C. H. Jiang, L. H. Lu, *Biomaterials* **2016**, *77*, 198.
39. J. Liu, W. B. Bu, S. J. Zhang, F. Chen, H. Y. Xing, L. M. Pan, L. P. Zhou, W. J. Peng, J. L. Shi, *Chem. Eur. J.* **2012**, *18*, 2335.
40. M. Liebi, S. Kuster, J. Kohlbrecher, T. Ishikawa, P. Fischer, P. Walde, E. J. Windhab, *J. Phys. Chem. B* **2013**, *117*, 14743.
41. D. Burdinski, J. A. Pikkemaat, J. Lub, P. de Peinder, L. N. Garrido, T. Weyhermuller, *Inorg. Chem.* **2009**, *48*, 6692.
42. K. Li, Y. H. Jiang, D. Ding, X. H. Zhang, Y. T. Liu, J. L. Hua, S. S. Feng, B. Liu, *Chem. Commun.* **2011**, *47*, 7323.
43 P. Horcajada, T. Chalati, C. Serre, B. Gillet, C. Sebrie, T. Baati, J. F. Eubank, D. Heurtaux, P. Clayette, C. Kreuz, J. S. Chang, Y. K. Hwang, V. Marsaud, P. N. Bories, L. Cynober, S. Gil, G. Fé rey, P. Couvreur, R. Gref, *Nat. Mater.* **2010,** *9*, 172.